

Sliding ferromagnetism in bilayer MnSiSe₃ and its application to spintronics

Jianing Tan,¹ Degao Xu,¹ Meng Ge,¹ Guowei Yang²,^{1,*} and Gang Ouyang^{1,*}

¹Key Laboratory of Low-Dimensional Quantum Structures and Quantum Control of Ministry of Education, Key Laboratory for Matter Microstructure and Function of Hunan Province, School of Physics and Electronics, Hunan Normal University, Changsha 410081, China

²State Key Laboratory of Optoelectronic Materials and Technologies, School of Materials Science and Engineering, Sun Yat-sen (Zhongshan) University, Guangzhou 510275, China

 (Received 26 May 2024; revised 11 August 2024; accepted 19 August 2024; published 3 September 2024)

Based on first-principles calculations, we report that the easy magnetization axis in two-dimensional (2D) van der Waals (vdW) magnets can be controlled by the sliding direction, a phenomenon we termed sliding ferromagnetism, directly linked to the second-order perturbation effects of spin-orbit coupling. Furthermore, we construct a MnSiSe₃/graphene-bilayer-BN-graphene/MnSiSe₃ vdW multiferroic tunnel junction (MFTJ) where the direction of sliding, rather than electric or magnetic fields, drives the device. Here, the sliding ferroelectric bilayer *h*-BN acts as the insulating area, and the sliding ferromagnetic mirrored-bilayer MnSiSe₃ serves as the electrodes. Our nonequilibrium Green's function calculations demonstrate the existence of multilevel resistance states in this MFTJ. These findings present an approach to manipulating the spin orientation in two-dimensional magnets without magnetic fields, and thus a colorful platform for designing tunable spintronic devices.

DOI: [10.1103/PhysRevB.110.125402](https://doi.org/10.1103/PhysRevB.110.125402)

I. INTRODUCTION

Controlling the orientation of magnetic moments is fundamental not only to the field of spintronics but also underpins its development. The tunnel junction is an important functional element with widespread applications in memory devices, sensors, and information processing systems [1–3]. The recent discoveries of two-dimensional (2D) magnetism and ferroelectrics offer promising avenues for designing miniaturized tunnel junctions [4–7]. For instance, multiferroic tunnel junctions (MFTJs) utilizing 2D magnetic metals and ferroelectric semiconductors have garnered significant interest [8–17]. The heightened attention originates from their inherently clean van der Waals (vdW) interfaces, reduced dimensionality, and the potential for more means of regulation compared to conventional MFTJs [18,19]. A considerable part of interest in 2D multiferroic materials stems from the expectation of achieving electrically controlled magnetism, thereby driving the development of spintronics [20,21].

Within the field of 2D ferroelectrics, the ferroelectricity in sliding systems has been theoretically predicted and experimentally confirmed [22–24], offering an innovative method for overcoming the difficulty of high-energy consumption associated with ferroelectric polarization switching. Likewise, within the realm of 2D magnets, various perturbations such as strain, polarization, spin polarization current, and electric or magnetic fields can alter the magnetic states [20,25–29]. In spintronics, all functional elements, such as spin valves and magnetic tunnel junctions, rely on manipulating the orientation of magnetic moment. However, a strategy akin to sliding ferroelectricity for efficiently manipulating spin orientation in 2D magnets with low-energy consumption is still lacking.

The monolayer MnSiSe₃, belonging to the transition-metal trichalcogenides family, is anticipated to exhibit a high Curie temperature and half-metallic properties [30,31]. Additionally, it is predicted that monolayer MnSiSe₃ displays an easy axis of magnetization in the in plane. We find that the sliding direction can control the easy magnetization axis in mirrored-bilayer MnSiSe₃. This phenomenon resembles sliding ferroelectricity, termed sliding ferromagnetism, and can be attributed to the second-order perturbation of spin-orbit coupling (SOC) in selenium atoms.

Furthermore, to verify the effectiveness of this manipulation method and preserve the large tunneling magnetoresistance (TMR) and tunneling electroresistance (TER) ratios in 2D vdW MFTJs, we construct a MFTJ by combining the concepts of sliding ferroelectricity and sliding ferromagnetism, wherein mirrored-bilayer MnSiSe₃ serves as the electrodes and bilayer *h*-BN as the insulating area [15,32]. In this sliding-driven vdW MFTJ with multilevel resistance states, we find the TMR and TER ratios can be up to 1009% and 508%, respectively.

In addition, we applied our strategy to other systems and obtained similar results, indicating that our approach is not limited to a single case. Our study suggests a significant approach to modify the orientation of magnetic moments without any external magnetic field and offers a promising platform to explore the spintronics applications.

II. COMPUTATIONAL METHODS

The first-principles calculations in this study are performed within the framework of density functional theory (DFT) [33], which is implemented in the Vienna *ab initio* simulation package with the projector augmented-wave (PAW) method [34–36]. We employ the Perdew-Burke-Ernzerhof (PBE) pseudopotential under the generalized

*Contact author: gangouy@hunnu.edu.cn

gradient approximation (GGA) and set the plane-wave cutoff energy to 500 eV, accompanied by a vacuum region of 20 Å along the z direction [37]. To describe the strong electron correlation in the Mn $3d$ states, we assign an effective U value of 4.0 eV [30,38]. The convergence criterion for the electronic energy and the Hellman-Feynman force are set to 10^{-6} eV and 0.001 eV/Å, respectively. We employ a Γ -centered k mesh with $12 \times 12 \times 1$ grids for self-consistent calculations, ensuring accurate energy estimation by restoring complete lattice symmetry under the GGA functional. Furthermore, the Grimme-D3 type of vdW force correction is considered in calculations [39], and SOC is integrated into the DFT calculations to determine the magnetocrystalline anisotropy energy (MAE).

The transport properties of MFTJs are calculated using the nonequilibrium Green's function (NEGF) method, as implemented in the NANODCAL software package [40,41]. A double- ζ polarized atomic-orbital basis was applied to all atoms, with the on-site effective Hubbard U parameter of 4 eV for $3d$ states of Mn atoms [42]. In the electronic self-consistent calculations, a grid of $10 \times 10 \times 100$ k points is employed for the electrodes, while a grid of $10 \times 10 \times 3$ k points was used for the central region. A $100 \times 100 \times 1$ k -point grid was applied to sample the Brillouin zone for the transport calculations, and the convergence test indicates that this k -point grid is sufficient (see Sec. 10 in the Supplemental Material for more details) [43]. An energy cutoff of 80 hartree was used in these calculations. The tunneling conductance can be obtained using the following equation [44,45],

$$G(E) = \frac{e^2}{h} T(E), \quad (1)$$

where e , h , and $T(E)$ denote the electron charge, Planck's constant, and the transmission coefficient, respectively. The orientation of magnetic moments and the ferroelectric polarization can be altered by applying proper sliding, whose manipulation yields multiple resistance states [e.g., parallel- and cross-magnetization configurations, see Fig. 4(d)]. In the equilibrium state, the TMR and TER ratios can then be defined as $\text{TMR} = (G_P - G_C)/G_C$, $\text{TER} = (G_\uparrow - G_\downarrow)/G_\downarrow$, where $G_{P/C}$ is the conductance in the parallel (P) and cross (C) magnetization configurations, and $G_{\uparrow/\downarrow}$ is the conductance of polarized configurations in the opposite directions.

III. RESULTS AND DISCUSSION

The MnSiSe₃ monolayer is characterized by a triangular lattice exhibiting the symmetry of the space group $P\bar{3}1m$, illustrated in Fig. 1(a). Assuming the MnSiSe₃ monolayer is parallel to the ab plane, the second layer arises from the stacking operator $\tau_z \hat{O}$, where τ_z is the out-of-plane translation operator and $\hat{O} = \{O|\tau_0\}$, with O as the rotational part, and τ_0 denotes the in-plane translational part presented in the form of fractional coordinates. In our case, we construct a mirrored-bilayer MnSiSe₃ using $O = m_z$. Figure 1(a) presents a series of translation points. The total energies of mirrored-bilayer MnSiSe₃ obtained using different τ_0 are calculated to determine the energy minima. As depicted in Fig. 1(b), the simply stacked bilayer [$\tau_0 = (0, 0)$] corresponds to the energy maximum, whereas shifting the second layer to the points A,

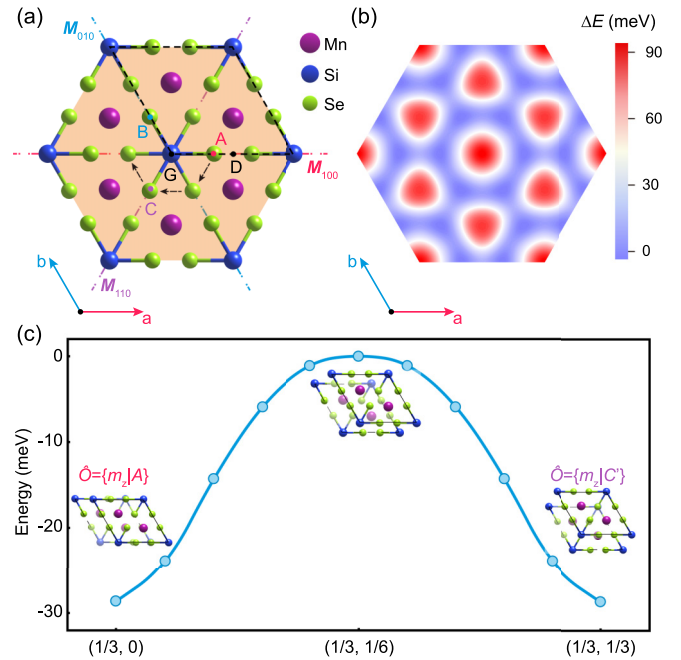


FIG. 1. (a) Top view of monolayer MnSiSe₃. The area surrounded by a black dashed line represents the unit cell. The high-symmetry translation points and the mirror plane (dashed-dotted line) are presented: G (0, 0), A (1/3, 0), B (0, 1/3), C (-1/3, -1/3), D (1/2, 0), and M (1/3, 2/3). (b) The energy difference between the different stacking orders of bilayer MnSiSe₃ [$\hat{O} = \{m_z|\tau_0\}$]. A , B , and C are the locations of the minima points of mirrored-bilayer MnSiSe₃. (c) The energy barrier between two structures correspond to the energy minima: A (1/3, 0) and C' (1/3, 1/3).

B , or C results in the threefold degenerate minima. The energy gap between the minima and maxima is -43.1 meV/f.u., indicating the favorable stable state at the minima. The energy barrier between the two stable state is 14 meV/f.u., as shown in Fig. 1(c), which has typical sliding characteristics with low-energy consumption.

The MnSiSe₃ monolayer is anticipated to exhibit a high Curie temperature with an in-plane easy magnetization axis [30]. Figure 2(a) illustrates the sixfold degenerate easy axis in the MnSiSe₃ monolayer, aligning with the D_{3d} symmetry of the MnSiSe₃ monolayer. We then systematically studied the MAE in bilayer MnSiSe₃ obtained using different \hat{O} ($O = E$ and m_z ; $\tau_0 = G, M, A, B, C,$ and D). Our results reveal that bilayer MnSiSe₃ shows an in-plane easy axis across all tested translation points, with the perpendicular MAE ranging from 3 to 6 meV (refer to Fig. S2 in the Supplemental Material for more details) [43]. Shifting the mirrored-top layer to the points of minimum energy ($O = m_z$; $\tau_0 = A, B,$ and C) results in a reduction in symmetry to C_s , subsequently leading to sliding ferromagnetism, i.e., the easy magnetization axis depends on the sliding direction [see Figs. 2(b)–2(d)]. Additionally, the in-plane MAE is computed at other test points, where the discrepancies are typically within the magnitude of μeV , indicating a lack of discernible spin orientation. Notably, although bilayer MnSiSe₃ displays an MAE of approximately 40 μeV under the operation $\hat{O} = \{E|A\}$, it remains significantly smaller than that of 1.7 mV exhibited in bilayer

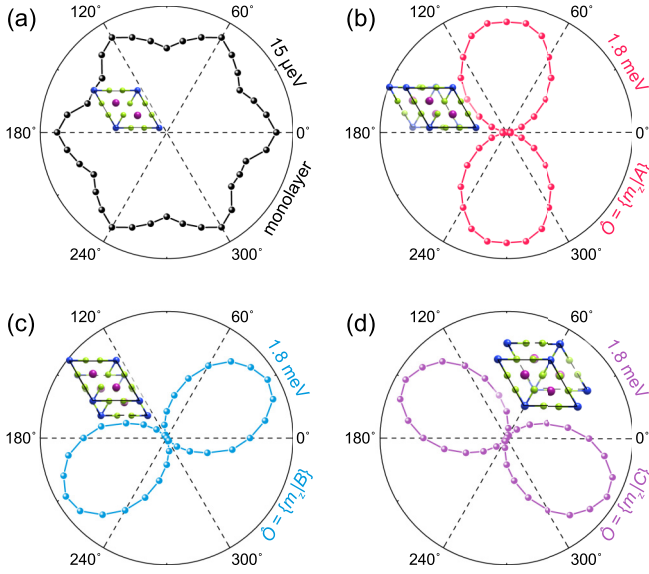


FIG. 2. Polar diagrams of the MAE of (a) MnSiSe₃ monolayer and bilayer MnSiSe₃ obtained using (b) $\hat{O} = \{m_z|A\}$, (c) $\hat{O} = \{m_z|B\}$, and (d) $\hat{O} = \{m_z|C\}$ in the xy plane.

MnSiSe₃ with the operation $\hat{O} = \{m_z|A\}$ [see Fig. 2(b) and Fig. S3(c) in the Supplemental Material for more details] [43]. In addition, we computed the variation in MAE throughout the sliding process. Through targeted path adjustments [the black dashed arrow in Fig. 1(a)], we achieved precise (360°) control over in-plane magnetic moments (see Fig. S4 in the Supplemental Material).

The MAE emerges from the SOC interaction, which can be estimated through second-order perturbation between occupied and unoccupied states [46–48],

$$E_O^{\tau_0, \varphi} = \frac{|\langle o | \hat{H}_{\text{SOC}} | u \rangle|^2}{\varepsilon_o - \varepsilon_u}, \quad (2)$$

where the φ , $|o\rangle$, $|u\rangle$, ε_o and ε_u stand for azimuth angle of magnetic moment, occupied states, unoccupied states, and corresponding energies, respectively. In our case, we examine two scenarios: one involving identical φ but varying τ_0 values ($\varphi = 0^\circ$; $\tau_0 = G, A$), and the other featuring identical τ_0 values but different φ ($\varphi = 0^\circ, 90^\circ$; $\tau_0 = A$). In fact, GA , GB , and GC represent three equivalent directions, owing to the D_{3h} symmetry of the simply stacked mirrored-bilayer MnSiSe₃ ($O = m_z$; $\tau_0 = G$). In the initial set of comparisons, the atomic-resolved and orbital-resolved SOC differences indicate that the MAE primarily originates from the $4p$ states of selenium atom, as illustrated in Fig. 3(a). All the elements make a negative contribution to MAE, with the hybridization between p_z and p_y states making the most significant impact due to the magnetization along the x direction ($\langle p_z | \hat{H}_{\text{SOC}} | p_y \rangle \sim \langle S_x \rangle$) [49], as shown in Fig. 3(b). In the second group, the scenario differs slightly from the first group. Specifically, not all selenium atoms make a negative contribution, but only those along the sliding direction [see Figs. 3(c) and S5 in the Supplemental Material for more details]. When the operation $\hat{O} = \{m_z|A\}$ is applied, $\langle p_z | \hat{H}_{\text{SOC}} | p_y \rangle \sim \langle S_x \rangle$ and $\langle p_z | \hat{H}_{\text{SOC}} | p_x \rangle \sim \langle S_y \rangle$ emerge as the primary sources of in-plane MAE in the mirrored-bilayer MnSiSe₃ as

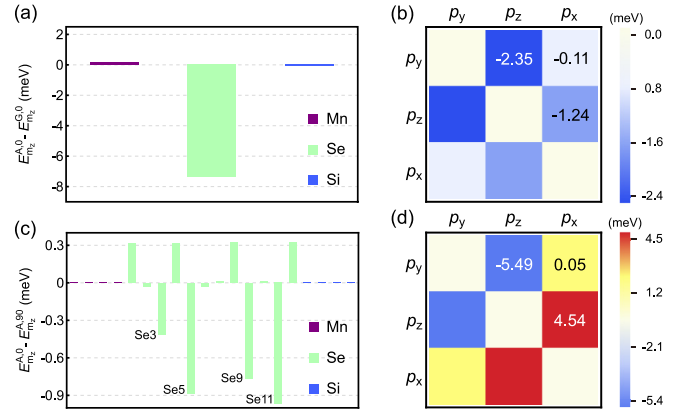


FIG. 3. The atomic-resolved SOC energy difference of bilayer MnSiSe₃ and (b) the orbital-resolved SOC energy difference of selenium atoms in bilayer MnSiSe₃, obtained using the operators $\hat{O} = \{m_z|G\}$ and $\hat{O} = \{m_z|A\}$, with both magnetic moments oriented along the x axis. (c) The atomic-resolved SOC energy difference of bilayer MnSiSe₃ and (d) the orbital-resolved SOC energy difference of selenium atoms in bilayer MnSiSe₃, calculated using the operator $\hat{O} = \{m_z|A\}$ with magnetic moments oriented differently: one along the x axis and the other along the y axis (e.g., $E_{m_z}^{A,90}$ represents the SOC energy of bilayer MnSiSe₃ obtained using the operator $\hat{O} = \{m_z|A\}$ and “90” represents the magnetic moment is perpendicular to x axis).

magnetization is along the x and y directions [49], respectively, as shown in Fig. 3(d). In our calculations, the magnetization expectation of the $4p$ state in selenium atom is consistent across both cases ($\sim 0.146 \mu_B$). Thus, the more negligible energy difference between p_z and p_y states compared to p_z and p_x states, as described in Eq. (2), is attributed to the emergence of sliding ferromagnetism.

It is worth noting that the total MAE (calculated from the total energy difference between distinct magnetic orientations) does not equal the sum of SOC energy differences from each atom, showing a discrepancy of 0.1 meV. This discrepancy arises from the limited applicability of second-order perturbation theory in metallic systems.

Figure 4(a) presents the spin-polarized electron structures of bilayer MnSiSe₃, acquired using the operator $\hat{O} = \{m_z|A\}$ without SOC. As observed with the monolayer, the ferromagnetic state of bilayer MnSiSe₃ remains a half metal, with bands near the Fermi level predominantly stemming from the $4p$ orbitals of the Se atom. Notably, the Weyl points opened a gap after sliding due to the break of certain mirror symmetries [e.g., M_{110} and M_{010} , see Fig. 1(a)]. We compared the spin direction resolved band structures of bilayer MnSiSe₃ obtained using the operator $\hat{O} = \{m_z|A\}$ and $\hat{O} = \{m_z|B\}$ with SOC. Figures 4(b) and 4(c) demonstrate the alteration of spin-majority and spin-minority states. Under the operator, $\hat{O} = \{m_z|A\}$, only electrons with spin in the x direction contribute to the bands. In contrast, under the operator, $\hat{O} = \{m_z|B\}$, contributions to the bands come from both the x and y directions. The conventional magnetic tunnel junction achieves a high TMR ratio by altering the distribution of spin-majority and spin-minority electrons via an external magnetic field [50]. Therefore, we aim to construct an MFTJ devoid of external

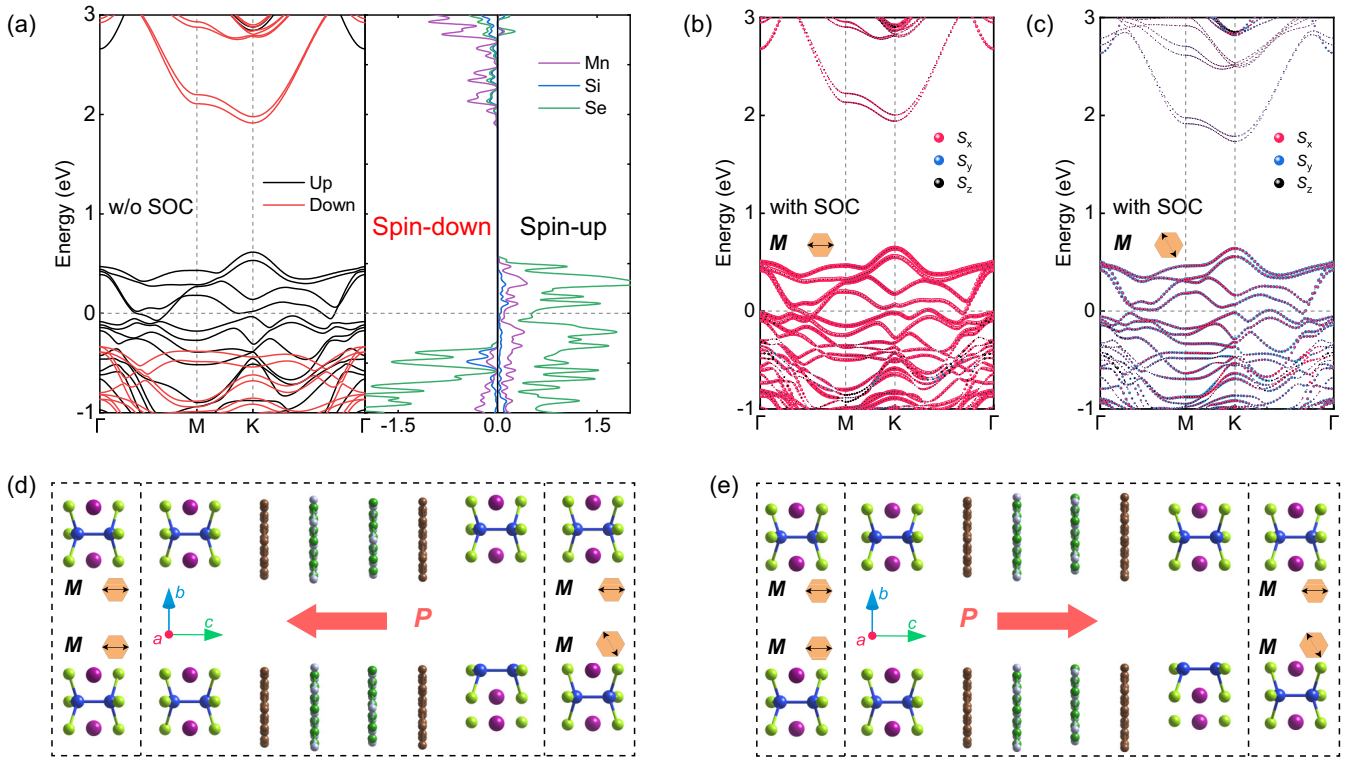


FIG. 4. The spin-polarized electron structures of bilayer MnSiSe₃ obtained using the operator $\hat{O} = \{m_z|A\}$. The spin direction resolved band structures of bilayer MnSiSe₃ obtained using the operator (b) $\hat{O} = \{m_z|A\}$, (c) $\hat{O} = \{m_z|B\}$. (d) and (e) are the side views of our MFTJ device models based on MnSiSe₃/Gr-bilayer-BN-Gr/MnSiSe₃. Both the polarization and the magnetization directions in the device can be altered by sliding.

electric and magnetic fields by integrating sliding ferroelectricity and sliding ferromagnetism.

As depicted in Figs. 4(d) and 4(e), an MFTJ exhibiting multilevel resistance states is constructed, where the electrode mirrored-bilayer MnSiSe₃ is paired with a bilayer *h*-BN serving as the insulating region. The supercells to build this MFTJ are 1×1 , $\sqrt{7} \times \sqrt{7}$, and $\sqrt{7} \times \sqrt{7}$ for bilayer MnSiSe₃ (6.374 Å), graphene (2.466 Å), and *h*-BN (2.511 Å), respectively. Given the research emphasis on sliding ferromagnetism, we adopt the in-plane lattice constant of bilayer MnSiSe₃ as the universal lattice constant for MFTJ, leading to compression of graphene and *h*-BN by 2.37% and 4.06%, respectively. In this MnSiSe₃/graphene-bilayer-BN-graphene/MnSiSe₃ vdW MFTJ, the graphene intercalation is employed to hinder the electron transfer between *h*-BN and MnSiSe₃ single layers, thereby diminishing the ferroelectric polarization in bilayer *h*-BN [15,32]. This MFTJ comprises two types of heterojunction interfaces: MnSiSe₃/graphene and graphene/*h*-BN. We conduct total energy evaluations for these interfaces considering various stacking orders, and one can find that Si/C and hollow/N are the energy-favorite configurations of MnSiSe₃/graphene and graphene/*h*-BN interfaces, respectively (see Fig. S6 in the Supplemental Material for more details) [43].

In the P configuration [$\hat{O} = \{m_z|A\}$]; see the upper part of Fig. 4(d)], the spin orientations of mirrored-bilayer MnSiSe₃ in both left and right electrodes align, while in the C configuration [$\hat{O} = \{m_z|A\}$ for the left, $\hat{O} = \{m_z|B\}$ for the right; see the lower part of Fig. 4(d)], the spin orientations of

mirrored-bilayer MnSiSe₃ in the left and right electrodes vary with the sliding direction. We designate it *ferroelectric I* (FE I) when the ferroelectric polarization in bilayer *h*-BN points from right to left. Conversely, we term it *ferroelectric II* (FE II) when the ferroelectric polarization points from left to right. As evident from Table I, the sliding of *h*-BN alters the ferroelectric polarization direction (FE I \rightarrow FE II), leading to a TER ratio of 508% (383%) in the P (C) magnetization configuration, and sliding of mirrored-bilayer MnSiSe₃ modifies the spin configuration (P \rightarrow C), yielding a TMR ratio of 1009% (780%) in the FE I (FE II) state. We also tested the absence of graphene intercalation. The maximum TMR (TER) ratio of MnSiSe₃/bilayer-BN/MnSiSe₃ vdW MFTJ is 1320% (13%) at the equilibrium state (see Table S1 in the Supplemental Material for more details) [43], which also illustrates the absence of ferroelectric polarization in the central region and is consistent with previous studies [32]. The transport properties of MnSiSe₃/Gr-bilayer-BN-Gr/MnSiSe₃ vdW MFTJ

TABLE I. Total conductance ($G_0 = 2e^2/h$), and TMR and TER ratios for the different multilevel resistance states of MnSiSe₃/Gr-bilayer-BN-Gr/MnSiSe₃ vdW MFTJ.

Configuration and ratio	FE I state	FE II state	TER
Parallel configuration	$1.43 \times 10^{-6} G_0$	$2.35 \times 10^{-7} G_0$	508%
Cross configuration	$1.29 \times 10^{-7} G_0$	$2.67 \times 10^{-8} G_0$	383%
TMR	1009%	780%	

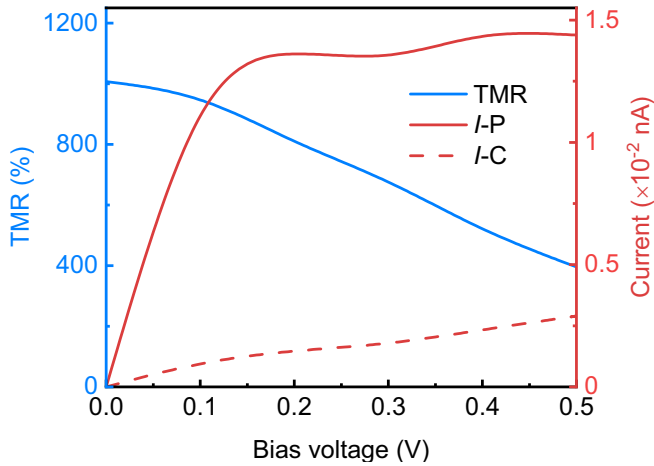


FIG. 5. The magnetoresistance (blue line), current of P (red line), and C (red dashed line) configuration vs the bias voltage of MnSiSe₃/Gr-bilayer-BN-Gr/MnSiSe₃ vdW MFTJs, where the TMR in the nonequilibrium state is calculated by current, $TMR = (I_P - I_C)/I_C$.

in a nonequilibrium state are also investigated. As shown in Fig. 5, the TMR ratio decreases with increasing bias, a trend consistent with our prior research [31].

We compared the differences of k_{\parallel} -resolved transmission coefficients with and without interlayering. Our calculations indicate that the interlayer thickens the central region, reducing the transmission coefficient. Furthermore, interlayered graphene facilitates additional tunneling pathways for electrons (see Fig. S10 in the Supplemental Material for more details) [43]. Alternatively, materials with multiple atomic layers can be selected as the barrier layer to mitigate the drawbacks associated with electron transfer, such as bilayer MoSi₂N₄. As depicted in Fig. 6, there are two polarization states in the central region of MnSiSe₃/bilayer-MoSi₂N₄/MnSiSe₃ vdW MFTJ. In the equilibrium state, the maximum TMR (TER) ratio of MnSiSe₃/bilayer-MoSi₂N₄/MnSiSe₃ vdW MFTJ reaches 833% (65%) (see Sec. 8 in Supplemental Material for more details, where the sliding ferroelectricity in bilayer MoSi₂N₄ and the transport property of MnSiSe₃/bilayer-MoSi₂N₄/MnSiSe₃ vdW MFTJ are discussed) [43]. The above results demonstrate that the TMR and TER ratios in sliding-dependent MFTJs can be effectively modulated.

IV. SUMMARY

In conclusion, we explore systematically the total energy and MAE of mirrored-bilayer MnSiSe₃ obtained using

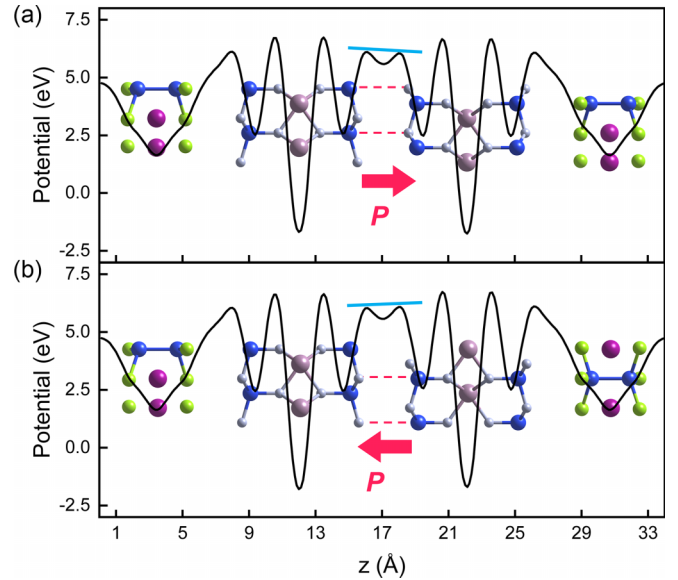


FIG. 6. The potential in the central region along the z axis for MnSiSe₃/bilayer-MoSi₂N₄/MnSiSe₃ vdW MFTJ. (a) The ferroelectric polarization points from left to right (FE II). (b) The ferroelectric polarization points from right to left (FE I).

different operators ($\hat{O} = \{O|\tau_0\}$) based on first-principles calculations. In previous studies [20,21], the approach for manipulating magnetism follows the sequence of interlayer sliding \rightarrow polarization \rightarrow controlled magnetism. Our strategy in this work discards intermediate processes, with magnetism being directly modulated via interlayer sliding. The underlying mechanism can be clarified by the second-order perturbation effects of SOC in Se atoms. Through constructing a MnSiSe₃/Gr-bilayer-BN-Gr/MnSiSe₃ vdW MFTJ, we find the functionality can be driven by sliding rather than external magnetic field. Following graphene intercalation, this MFTJ shows enhanced performance with the TMR (TER) ratio up to 1009% (508%). Our study provides an approach to manipulate the spin orientation in 2D vdW magnetic materials.

ACKNOWLEDGMENTS

We gratefully acknowledge HZWTECH for providing computation facilities. This work was supported by the National Natural Science Foundation of China (Grants No. U2001215 and 12474226) and the Postgraduate Scientific Research Innovation Project of Hunan Province (CX20240529).

- [1] S. A. Wolf, D. D. Awschalom, R. A. Buhrman, J. M. Daughton, S. von Molnár, M. L. Roukes, A. Y. Chtchelkanova, and D. M. Treger, Spintronics: A spin-based electronics vision for the future, *Science* **294**, 1488 (2001).
- [2] C.-G. Duan, S. S. Jaswal, and E. Y. Tsymlal, Predicted magnetoelectric effect in Fe/BaTiO₃ ultralayers: Ferroelectric control of magnetism, *Phys. Rev. Lett.* **97**, 047201 (2006).

- [3] E. Y. Tsymlal and H. Kohlstedt, Tunneling across a ferroelectric, *Science* **313**, 181 (2006).
- [4] A. Belianinov, Q. He, A. Dziazugys, P. Maksymovych, E. Eliseev, A. Borisevich, A. Morozovska, J. Banys, Y. Vysochanskii, and S. V. Kalinin, CuInP₂S₆ room temperature layered ferroelectric, *Nano Lett.* **15**, 3808 (2015).
- [5] B. Huang, G. Clark, E. Navarro-Moratalla, D. R. Klein, R. Cheng, K. L. Seyler, D. Zhong, E. Schmidgall, M. A. McGuire,

- D. H. Cobden, W. Yao, D. Xiao, P. Jarillo-Herrero, and X. Xu, Layer-dependent ferromagnetism in a van der Waals crystal down to the monolayer limit, *Nature (London)* **546**, 270 (2017).
- [6] C. Gong, L. Li, Z. Li, H. Ji, A. Stern, Y. Xia, T. Cao, W. Bao, C. Wang, Y. Wang, Z. Q. Qiu, R. J. Cava, S. G. Louie, J. Xia, and X. Zhang, Discovery of intrinsic ferromagnetism in two-dimensional van der Waals crystals, *Nature (London)* **546**, 265 (2017).
- [7] W. Ding, J. Zhu, Z. Wang, Y. Gao, D. Xiao, Y. Gu, Z. Zhang, and W. Zhu, Prediction of intrinsic two-dimensional ferroelectrics in In_2Se_3 and other $\text{III}_2\text{-VI}_3$ van der Waals materials, *Nat. Commun.* **8**, 14956 (2017).
- [8] Y. Su, X. Li, M. Zhu, J. Zhang, L. You, and E. Y. Tsymbal, Van der Waals multiferroic tunnel junctions, *Nano Lett.* **21**, 175 (2021).
- [9] Z. Yan, Z. Li, Y. Han, Z. Qiao, and X. Xu, Giant tunneling magnetoresistance and electroresistance in $\alpha\text{-In}_2\text{Se}_3$ -based van der Waals multiferroic tunnel junctions, *Phys. Rev. B* **105**, 075423 (2022).
- [10] L. Shu, L. Qian, X. Ye, and Y. Xie, Multifunctional two-dimensional $\text{VSi}_2\text{N}_4/\text{WSi}_2\text{N}_4/\text{VSi}_2\text{N}_4$ photodetector driven by the photogalvanic effect, *Phys. Rev. Appl.* **17**, 054010 (2022).
- [11] X. Yu, X. Zhang, and J. Wang, Fully electrically controlled van der Waals multiferroic tunnel junctions, *ACS Nano* **17**, 25348 (2023).
- [12] Y. Zhang, X. Li, J. Sheng, S. Yu, J. Zhang, and Y. Su, Multilevel resistance states in van der Waals multiferroic tunnel junctions above room temperature, *Appl. Phys. Lett.* **123**, 192402 (2023).
- [13] H. Hu, D. Xu, and G. Ouyang, Interface design for the transport properties in asymmetric two-dimensional van der Waals multiferroic tunnel junctions, *Phys. E* **145**, 115501 (2023).
- [14] B. Liu, X. X. Ren, X. Zhang, P. Li, Y. Dong, and Z.-X. Guo, Electric field tunable multi-state tunnel magnetoresistances in 2D van der Waals magnetic heterojunctions, *Appl. Phys. Lett.* **122**, 152408 (2023).
- [15] X. Dong, X. Shen, X. Sun, Y. Bai, Z. Yan, and X. Xu, Voltage-tunable giant nonvolatile multiple-state resistance in sliding-interlayer ferroelectric $h\text{-BN}$ van der Waals multiferroic tunnel junction, *Phys. Rev. B* **108**, 085427 (2023).
- [16] Z. Cui, B. Sa, K.-H. Xue, Y. Zhang, R. Xiong, C. Wen, X. Miao, and Z. Sun, Magnetic-Ferroelectric synergic control of multilevel conducting states in van der Waals multiferroic tunnel junctions towards in-memory computing, *Nanoscale* **16**, 1331 (2024).
- [17] Y. Feng, J. Han, K. Zhang, X. Lin, G. Gao, Q. Yang, and S. Meng, van der Waals multiferroic tunnel junctions based on sliding multiferroic layered VSi_2N_4 , *Phys. Rev. B* **109**, 085433 (2024).
- [18] J. P. Velev, C.-G. Duan, J. D. Burton, A. Smogunov, M. K. Niranjana, E. Tosatti, S. S. Jaswal, and E. Y. Tsymbal, Magnetic tunnel junctions with ferroelectric barriers: Prediction of four resistance states from first principles, *Nano Lett.* **9**, 427 (2009).
- [19] M. Ye, Zhuravlev, S. Maekawa, and E. Y. Tsymbal, Effect of spin-dependent screening on tunneling electroresistance and tunneling magnetoresistance in multiferroic tunnel junctions, *Phys. Rev. B* **81**, 104419 (2010).
- [20] X. Liu, A. P. Pyatakov, and W. Ren, Magnetoelectric coupling in multiferroic bilayer VS_2 , *Phys. Rev. Lett.* **125**, 247601 (2020).
- [21] K. Liu, X. Ma, S. Xu, Y. Li, and M. Zhao, Tunable sliding ferroelectricity and magnetoelectric coupling in two-dimensional multiferroic MnSe materials, *npj Comput. Mater.* **9**, 16 (2023).
- [22] L. Li and M. Wu, Binary compound bilayer and multilayer with vertical polarizations: Two-dimensional ferroelectrics, multiferroics, and nanogenerators, *ACS Nano* **11**, 6382 (2017).
- [23] K. Yasuda, X. Wang, K. Watanabe, T. Taniguchi, and P. Jarillo-Herrero, Stacking-engineered ferroelectricity in bilayer boron nitride, *Science* **372**, 1458 (2021).
- [24] J. Ji, G. Yu, C. Xu, and H. J. Xiang, General theory for bilayer stacking ferroelectricity, *Phys. Rev. Lett.* **130**, 146801 (2023).
- [25] Y. Deng, Y. Yu, Y. Song, J. Zhang, N. Z. Wang, Z. Sun, Y. Yi, Y. Z. Wu, S. Wu, J. Zhu, J. Wang, X. H. Chen, and Y. Zhang, Gate-tunable room-temperature ferromagnetism in two-dimensional Fe_3GeTe_2 , *Nature (London)* **563**, 94 (2018).
- [26] T. Li, S. Jiang, N. Sivadas, Z. Wang, Y. Xu, D. Weber, J. E. Goldberger, K. Watanabe, T. Taniguchi, C. J. Fennie, K. Fai Mak, and J. Shan, Pressure-controlled interlayer magnetism in atomically thin CrI_3 , *Nat. Mater.* **18**, 1303 (2019).
- [27] E. Grimaldi, V. Krizakova, G. Sala, F. Yasin, S. Couet, G. Sankar Kar, K. Garello, and P. Gambardella, Single-shot dynamics of spin-orbit torque and spin transfer torque switching in three-terminal magnetic tunnel junctions, *Nat. Nanotechnol.* **15**, 111 (2020).
- [28] Z. Ni, A. V. Haglund, H. Wang, B. Xu, C. Bernhard, D. G. Mandrus, X. Qian, E. J. Mele, C. L. Kane, and L. Wu, Imaging the Néel vector switching in the monolayer antiferromagnet MnPSe_3 with strain-controlled Ising order, *Nat. Nanotechnol.* **16**, 782 (2021).
- [29] G. Wang, K. Yang, Y. Ma, L. Liu, D. Lu, Y. Zhou, and H. Wu, Superexchange interactions and magnetic anisotropy in MnPSe_3 monolayer, *Chin. Phys. Lett.* **40**, 077301 (2023).
- [30] B. L. Chittari, D. Lee, N. Banerjee, A. H. MacDonald, E. Hwang, and J. Jung, Carrier- and strain-tunable intrinsic magnetism in two-dimensional MAX_3 transition metal chalcogenides, *Phys. Rev. B* **101**, 085415 (2020).
- [31] J. Tan, G. Yang, and G. Ouyang, Large tunneling magnetoresistance and its high bias stability in Weyl half-semimetal based lateral magnetic tunnel junctions, *New J. Phys.* **26**, 033047 (2024).
- [32] J. Yang, J. Zhou, J. Lu, Z. Luo, J. Yang, and L. Shen, Giant tunnelling electroresistance through 2D sliding ferroelectric materials, *Mater. Horiz.* **9**, 1422 (2022).
- [33] P. Hohenberg and W. Kohn, Inhomogeneous electron gas, *Phys. Rev.* **136**, B864 (1964).
- [34] G. Kresse and J. Hafner, *Ab initio* molecular dynamics for liquid metals, *Phys. Rev. B* **47**, 558 (1993).
- [35] G. Kresse and J. Furthmüller, Efficient iterative schemes for *ab initio* total-energy calculations using a plane-wave basis set, *Phys. Rev. B* **54**, 11169 (1996).
- [36] P. E. Blöchl, Projector augmented-wave method, *Phys. Rev. B* **50**, 17953 (1994).
- [37] J. P. Perdew, K. Burke, and M. Ernzerhof, Generalized gradient approximation made simple, *Phys. Rev. Lett.* **77**, 3865 (1996).
- [38] D. Zhang, A. Rahman, W. Qin, X. Li, P. Cui, Z. Zhang, and Z. Zhang, Prediction of MnSiTe_3 as an intrinsic layered half-metal, *Phys. Rev. B* **101**, 205119 (2020).
- [39] S. Grimme, J. Antony, S. Ehrlich, and H. Krieg, A consistent and accurate *ab initio* parametrization of density functional

- dispersion correction (DFT-D) for the 94 elements H-Pu, *J. Chem. Phys.* **132**, 154104 (2010).
- [40] J. Taylor, H. Guo, and J. Wang, *Ab initio* modeling of quantum transport properties of molecular electronic devices, *Phys. Rev. B* **63**, 245407 (2001).
- [41] J. Taylor, H. Guo, and J. Wang, *Ab initio* modeling of open systems: Charge transfer, electron conduction, and molecular switching of a C₆₀ device, *Phys. Rev. B* **63**, 121104(R) (2001).
- [42] V. I. Anisimov, F. Aryasetiawan, and A. I. Lichtenstein, First-principles calculations of the electronic structure and spectra of strongly correlated systems: The LDA + *U* method, *J. Phys.: Condens. Matter* **9**, 767 (1997).
- [43] See Supplemental Material at <http://link.aps.org/supplemental/10.1103/PhysRevB.110.125402> for the energy difference of MnSiSe₃ under the simple stack; the magnetocrystalline anisotropy energy of bilayer MnSiSe₃; total energy evaluations for different interfaces at various stacking orders; the transport property of other vdW MFTJs; sliding ferromagnetism in bilayer CrI₃ and bilayer VSi₂N₄; and the convergence test of the transport property.
- [44] Y. Meir and N. S. Wingreen, Landauer formula for the current through an interacting electron region, *Phys. Rev. Lett.* **68**, 2512 (1992).
- [45] A.-P. Jauho, N. S. Wingreen, and Y. Meir, Time-dependent transport in interacting and noninteracting resonant-tunneling systems, *Phys. Rev. B* **50**, 5528 (1994).
- [46] D.-S. Wang, R. Wu, and A. J. Freeman, First-principles theory of surface magnetocrystalline anisotropy and the diatomic-pair model, *Phys. Rev. B* **47**, 14932 (1993).
- [47] D.-S. Wang, R. Wu, and A. J. Freeman, State-tracking first-principles determination of magnetocrystalline anisotropy, *Phys. Rev. Lett.* **70**, 869 (1993).
- [48] G. van der Laan, Microscopic origin of magnetocrystalline anisotropy in transition metal thin films, *J. Phys.: Condens. Matter* **10**, 3239 (1998).
- [49] S. Kunschuh, M. Gmitra, and J. Fabian, Tight-binding theory of the spin-orbit coupling in graphene, *Phys. Rev. B* **82**, 245412 (2010).
- [50] M. Julliere, Tunneling between ferromagnetic films, *Phys. Lett. A* **54**, 225 (1975).